JOURNAL OF COMPUTATIONAL PHYSICS **146,** 105–123 (1998)
ARTICLE NO. CP986042

Three-Dimensional Computation of Bubbles Near a Free Surface

Y. L. Zhang, K. S. Yeo, B. C. Khoo, and W. K. Chong

Department of Mechanical and Production Engineering, National University of Singapore, Kent Ridge, Singapore 119260, Republic of Singapore
E-mails: mpezyl@leonis.nus.sg, mpeyeoks@nus.sg, mpekbc@nus.sg, mpecwk@leonis.nus.sg

Received January 21, 1997; revised May 1, 1998

A new boundary element model for simulating the interaction of one or more bubbles and a free surface is described. An important feature of this model is the utilization of a nine-noded Lagrangian interpolation for the computation of surface characteristics and material velocity. Solid angles on the free surface are computed via a direct approach, as opposed to the indirect approach usually employed for closed surfaces. The evolution of the bubble is followed until the point before the reentrant jet impacts on the opposite wall of the bubble. The results of the 3D code are compared against those of a one-dimensional Rayleigh–Plesset model and an axisymmetric code. New results are presented for the interaction of two bubbles and a free surface, where fully three-dimensional features are expected.

Key Words: integral equations; potential theory.

1. INTRODUCTION

In the area of bubbles dynamics, which has important applications in a number of engineering fields such as cavitation and underwater explosions, the most successful approach so far is the boundary element method (BEM) based on the Green's direct representation [11], coupled with some time-stepping scheme. One of the key issues in the implementation of this direct formulation is the accurate determination of the material velocity of the surfaces, following the solution of the boundary-integral equation. The problem is presented by the nonsmooth nature of the discretized surface, which entails the use of a local or global surface interpolation scheme to define the normal direction and tangential plane. Previous works on 3D bubble dynamics can be reviewed in this light. Harris [1] used an averaging of linear approximations on the surface elements. But as noted by Blake *et al.* [2], this algorithm suffers from the nonconvergence problem under the mesh refinement. Chahine *et al.* [3, 4] used quadratic polynomials to fit the surface locally, but his method fails for

0021-9991/98 $25.00

certain arrangements of the nodes such as a sphere for which the coefficient matrix is not of full rank (cf. [2]). Following this line, Blake *et al.* [2] proposed a number of local interpolation functions, one of which, the radial basis functions, was claimed to be universally applicable. However, even for this type of shape functions, the local interpolating surfaces has the form of $z = f(x, y)$, where (x, y, z) are the coordinates of a Cartesian frame. For certain points, when the bubble surface is parallel or nearly parallel to the z-axis, this would render the mapping singular or nearly singular. To overcome this problem, the Cartesian frame would have to be reorientated to keep the interpolating map locally diffeomorphic. This may be cumbersome, especially in some complicated cases involving the interaction of multiple bubbles, structures, and free surfaces where one does not know *a priori* when and which part of the moving surfaces would become parallel to the z-axis. In this regard, Zinchenko *et al.* [5] utilized a local Cartesian frame, obtained from an iterative method, with the z-axis pointing in the normal direction. A least-square method was then used to fit the local surface with quadratic functions. This method, however, becomes less accurate when the number of neighboring nodes far exceeds 4. Other 3D studies include those of Wilkerson [6], Chahine [7], Harris [8], Blake and Tong [9] and Chen *et al.* [10].

An alternative scheme of surface interpolation is employed in this paper to compute the material velocity of the bubble surface. Local interpolation is carried out via the shape functions of a 9-noded Lagrangian element. Such element has been used by Brebbia *et al.* [11] and others in the context of other BEM applications. The interpolant is trivariate in nature and may be applied in a uniform fashion to any local surface patch regardless of the orientation of the latter to the global axes. Moreover, with this interpolation algorithm, we are also able to obtain the material velocity (all its Cartesian components) of the surface directly, instead of calculating its normal and tangential component separately, as previous authors have done. The convergence of the algorithm is verified with a bubble of spherical symmetry.

Then we incorporate this algorithm into a 3D BEM code to study the interaction of bubbles and a free surface. We also propose an effective direct procedure for computing the nodal solid angles on the free surface. For axisymmetric cases, our results compare favorably with those from an axisymmetric model. Finally, we present the results of two cases in which 3D effects are dominant. For brevity, only the results for cavitation bubbles are presented in this paper although the extension of the current model to gas-filled bubbles is straightforward.

2. MATHEMATICAL FORMULATION

The most fundamental assumption used here is that the fluid is inviscid and incompressible and the induced motion irrotational. Therefore a potential function $\phi(x, y, z)$ exists in the region occupied by the fluid, which is bounded by some bubbles and a free surface. A Cartesian co-ordinate system $Oxyz$ is used with the Oxy plane coinciding with the undisturbed free surface. Then the Green's second identity reads

$$c(P)\phi(P) + \int_S \left[\phi(Q)\frac{\partial G(P, Q)}{\partial n(Q)} - \frac{\partial \phi(Q)}{\partial n(Q)} G(P, Q)\right] \mathrm{d}S(Q) = 0, \tag{1}$$

where $P = (x, y, z)$ is the control point, $Q = (x', y', z')$ is the integration point, $G(P, Q) = |\vec{PQ}|^{-1}$ is the free space Green's function, $c(P)$ is a geometrical parameter associated with

the solid angle (which is the conventional internal angle in 2D cases), $\mathbf{n}$ is the unit normal pointing out of the fluid region, and S is the sum of all boundaries which are discretized into triangular elements. Linear interpolation is used for the potential function and its normal derivative (Brebbia *et al*. [11]). The discretization scheme on the initially spherical bubbles and the quadrature used for the integration of the surface integral can be found in Wilkerson [6].

For cavitation bubbles, the evolution equations are

$$\frac{D\mathbf{r}}{Dt} = \nabla\phi, \tag{2}$$

$$\frac{D\phi}{Dt} = \frac{1}{2}|\nabla\phi|^2 - gz \text{ on the free surface}, \tag{3}$$

$$\frac{D\phi}{Dt} = \frac{p_\infty - p_c}{\rho} + \frac{1}{2}|\nabla\phi|^2 - g(z-\gamma') \text{ on a bubble surface}, \tag{4}$$

where the terms on the left-hand side are material derivatives, $\mathbf{r} = (x, y, z)$ is the position vector, ∇ is the gradient operator, g is the gravitational acceleration, p_c is the constant pressure inside the bubble. The center of the spherical bubble at inception is on the plane $z = \gamma'$ and p_∞ is the ambient pressure on this plane. In addition, a boundary condition must be prescribed in the far field:

$$\phi \to 0, \quad r = \sqrt{x^2 + y^2 + z^2} \to \infty. \tag{5}$$

We then proceed to nondimensionalize variables with the length scale being R_m (maximum radius of one of the bubbles) and the time scale being $R_m\sqrt{\rho/(p_\infty - p_c)}$. The nondimensionalized Bernoulli equations then become

$$\frac{D\phi}{Dt} = \frac{1}{2}|\nabla\phi|^2 - \delta^2 z \qquad \text{on the free surface}, \tag{6}$$

$$\frac{D\phi}{Dt} = 1 + \frac{1}{2}|\nabla\phi|^2 - \delta^2(z-\gamma) \quad \text{on the bubble surface}, \tag{7}$$

with $\delta = [\rho g R_m/(p_\infty - p_c)]^{1/2}$ being the buoyancy parameter. We have neglected the surface tension effects in the above formulation for the sake of simplicity. Blake *et al*. [15] have noted that for large bubbles (millimeter or larger), the surface tension effects are generally insignificant over much of the bubble's lifetime. For very small bubbles, surface tension effects can be significant and in this case, the above formulation should be modified to accommodate the effects if necessary.

The initial conditions are derived by integrating the Rayleigh–Plesset equation from the time of inception to the time when the bubble growth is arrested. For cavitation bubbles, the initial value of the potential on the bubble, whose radius is assumed to be $\frac{1}{10}$ of the maximum radius, is given by (cf. [16])

$$\phi(t_0) = -2.58 \quad \text{at } t_0 = 0.0015527. \tag{8}$$

2.1. *Calculation of Material Velocity*

It can be seen from (2) to (4) that the material velocity is needed to advance the solution. As stated in Section 1, a number of local interpolation schemes have been proposed, but

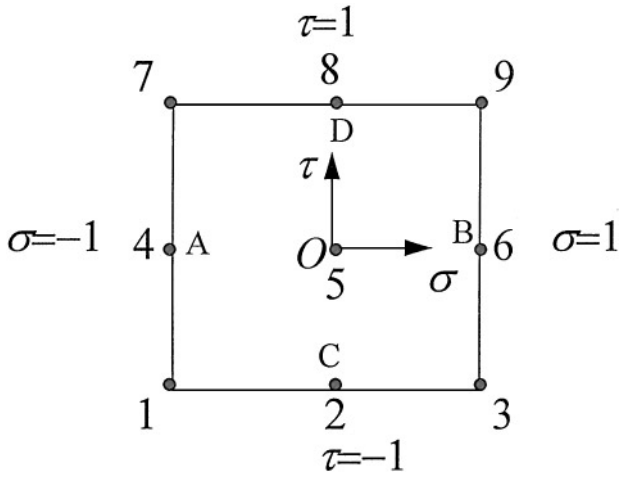

FIG. 1. Nine-noded Lagrangian element and the local curvilinear system (σ, τ).

none of them are fully satisfactory. Here we make use of the interpolation functions used in the nine-noded Lagrangian element (Brebbia *et al*. [11]). Referring to Fig. 1, the quadratic surface that passes through all the nine nodes and the interpolation functions associated with each node are given in terms of the curvilinear coordinates (σ, τ) as

$$\mathbf{r} = \sum_{i=1}^{9} f_i \mathbf{r}_i, \tag{9}$$

$$u = \sum_{i=1}^{9} f_i u_i, \tag{10}$$

$$f_1 = \frac{1}{4}\sigma(\sigma-1)\tau(\tau-1), \tag{11}$$

$$f_2 = \frac{1}{2}(1-\sigma^2)\tau(\tau-1), \tag{12}$$

$$f_3 = \frac{1}{4}\sigma(\sigma+1)\tau(\tau-1), \tag{13}$$

$$f_4 = \frac{1}{2}\sigma(\sigma-1)(1-\tau^2), \tag{14}$$

$$f_5 = (1-\sigma^2)(1-\tau^2), \tag{15}$$

$$f_6 = \frac{1}{2}\sigma(\sigma+1)(1-\tau^2), \tag{16}$$

$$f_7 = \frac{1}{4}\sigma(\sigma-1)\tau(\tau+1), \tag{17}$$

$$f_8 = \frac{1}{2}(1-\sigma^2)\tau(\tau+1), \tag{18}$$

$$f_9 = \frac{1}{4}\sigma(\sigma+1)\tau(\tau+1), \tag{19}$$

where $\mathbf{r}$ and $\mathbf{r}_i$ are position vectors, u is any scalar function defined locally. It can be verified that $f_i(j) = \delta_{ij}$ $(1 \le i, j \le 9)$ with δ_{ij} being the Kronecker delta, where j denotes

the j-node, and that $\sum_{i=1}^{9} f_i = 1$, which means that there is no interpolation error for u, if u is a linear function of x, y, z, and for the fitted surface, if all the nine nodes are coplanar. With the scheme, a local curvilinear frame is automatically conferred to the nodal points in question via the standard element. Therefore no explicit construction or selection of reference frame for interpolation is required. It should also be noted that the nine nodes need not be distinct.

Suppose that the velocity at the central node 5 is required. Then we have the relations for the derivatives along two tangential directions and the normal direction,

$$\left.\begin{aligned} ux_\sigma + vy_\sigma + wz_\sigma &= \tfrac{\partial\phi}{\partial\sigma} \\ ux_\tau + vy_\tau + wz_\tau &= \tfrac{\partial\phi}{\partial\tau} \\ un_x + vn_y + wn_z &= \tfrac{\partial\phi}{\partial n} \end{aligned}\right\} \quad \text{at } \sigma = \tau = 0, \tag{20}$$

where u, v, and w are the Cartesian components of the velocity vector. The coefficients $(x_\sigma, y_\sigma, z_\sigma) = \frac{1}{2}(x_6 - x_4, y_6 - y_4, z_6 - z_4) = \frac{1}{2}\mathbf{AB}$, $(x_\tau, y_\tau, z_\tau) = \frac{1}{2}(x_8 - x_2, y_8 - y_2, z_8 - z_2) = \frac{1}{2}\mathbf{CD}$, and $\frac{\partial\phi}{\partial\sigma} = (\phi_6 - \phi_4)/2$, $\frac{\partial\phi}{\partial\tau} = (\phi_8 - \phi_2)/2$ are the velocities along the direction σ and τ; $\partial\phi/\partial n$ is obtained from the solution of the boundary integral equation, and the normal vector $\mathbf{n} = \pm\mathbf{AB} \times \mathbf{CD}$ (the sign is chosen such that $\mathbf{n}$ is outward normal), $(n_x, n_y, n_z) = \mathbf{n}/|\mathbf{n}|$. Solving Eqs. (20) gives the material velocity vector (u, v, w) of the surface directly. Therefore, unlike previous models (e.g., Blake *et al*. [2]), where the normal and tangential velocities were calculated separately with the tangential velocity being computed by further assumptions and approximations, our method allows the three components of the material velocity to be computed simultaneously in a consistent and unambiguous fashion. It can be shown that the determinant of the coefficient matrix is $\pm|\mathbf{n}|/4$, and thus, the linear system has a solution if $|\mathbf{n}| \neq 0$.

Depending on the location of a node on the surface, there may be five or six elements surrounding the node, and thus lumping or addition of nodes is frequently necessary. These two situations are illustrated in Fig. 2, together with our arrangement of the Lagrangian nodes 1–9. The values of the potential function at the added Lagrangian nodes are found by linear interpolation, which is consistent with the linear interpolation used in each element. Node lumping or element degeneration is an accepted practice for functional interpolation [17]. It can produce singularities for the first derivatives at the lumped nodes, but the interpolant is first-order smooth away from the degenerated nodes. Since the surface point in question is the central node 5, which is never lumped with other nodes, a locally smooth and regular surface is expected around this node.

While element degeneration may sometimes have adverse effect on accuracy, it does not, however, decrease the formal *order of accuracy* of the interpolants, which remains second-order. Therefore, grid convergence to the solution is not affected by lumping of nodes. Interpolation inaccuracy may also arise when the mesh around the central node is highly distorted. But this is true of all methods, since the results of a procedure may only be as accurate as the regularity of data allows. Loss of accuracy due to mesh distortion, however, may be rectified, if necessary, by suitable mesh refinement.

Since the value of the potential function within each element is defined based on a linear interpolation of its nodal values, first-order convergence for the computed velocities is therefore expected. While the linear interpolation of ϕ appears to be adequate for the present study, the nine-noded Lagrangian interpolant may also be extended to the potential function in the usual isoparametric manner.

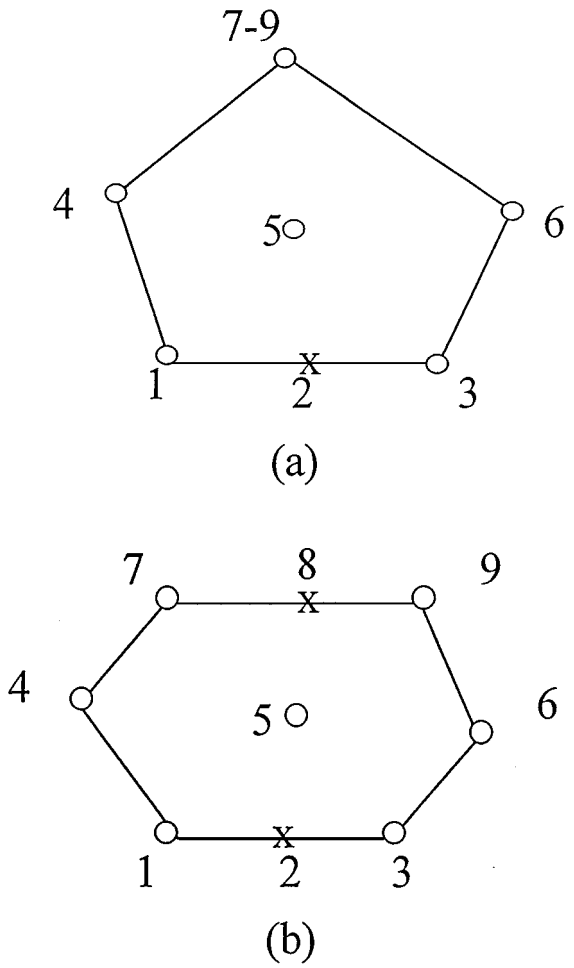

FIG. 2. Two outlines of the local nodes used in the local interpolation scheme and the designated numbers corresponding to a Lagrangian element: "o," original nodes; "×," added Lagrangian nodes. The nodes may not be coplanar.

2.2. *Time Stepping*

We adopt a forward-difference scheme for the time stepping. The time step, however, needs to be carefully chosen to curb the instability and truncation errors. Unlike axisymmetric cases where the sawtooth instability is commonly present, the 3D time stepping was found to be quite stable. Only when the jet is fully developed and comes very close to the opposite wall of the bubble did we encounter some numerical instability.

Stability is not the only concern in a numerical scheme; the time step must be carefully chosen such that the truncation errors will be kept small. Gibson and Blake [12] proposed that the time step be chosen in such a way that the maximum change of the potential ϕ in each time step is restricted by a constant $\Delta\phi$. Here we use a criterion slightly different from that of Chahine and Duraiswami [13] that the maximum change of the length of each side of the triangular elements is restricted by certain percentage ϵ ($= 4\%$ in this paper).

To validate the new criterion, we first compare the performance of the two aforementioned criteria to choose the time step. Shown in Fig. 3 are the results for the interaction between one

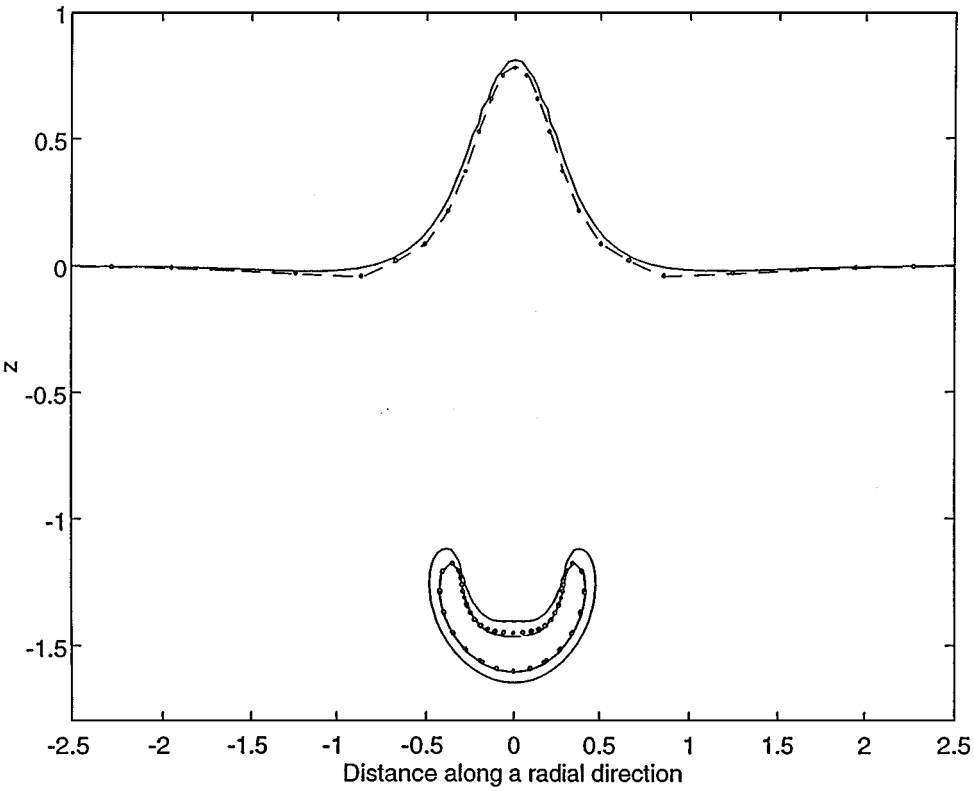

FIG. 3. Comparison of the bubble and free surface shapes for $\gamma = 1$ and $\delta = 0$ at $t = 1.4206$ calculated from our method of choosing time step with a tolerance $\epsilon = 4\%$ (dash lines), from Gibson and Blake's method with $\Delta\phi = 0.04$ (circles), and from an axisymmetric model in Wang *et al*. (solid lines).

bubble and a free surface. It is seen that the final results, including the jet configuration and the free-surface hump, are of similar accuracy and compare well with the results generated from the axisymmetric code of Wang *et al*. [14]. But with the new criterion 5% CPU time is saved. Although the saving in this case is only marginal, our test run for the interaction between a bubble and a solid wall indicates that more than 50% CPU time is saved with the new criterion. The reason for this is that, for the latter case, the time steps calculated from the new criterion are unusually large when the bubble grows closer to its maximum volume (with small material velocities); on the other hand, in the case of a bubble and a free surface, the motion on the free surface has significantly reduced the time steps when the bubble volume is close to its maximum. The saving of CPU time is greatly appreciated since for cases involving multiple bubbles and a free surface the CPU time may run up to several days on a Cray J916 computer system because of the large number of nodes involved in the computation.

2.3. *Calculation of Solid Angles on the Free Surface*

When a free surface is present, we encounter another difficulty, i.e. the calculation of the solid angle $c(P)$. For a closed surface, one can always calculate it via other entries of the influence matrix (cf. Brebbia *et al*. [11]). But the free surface is not closed. Of course, one way to circumvent this hurdle is to add some artificial surfaces to the free surface to render

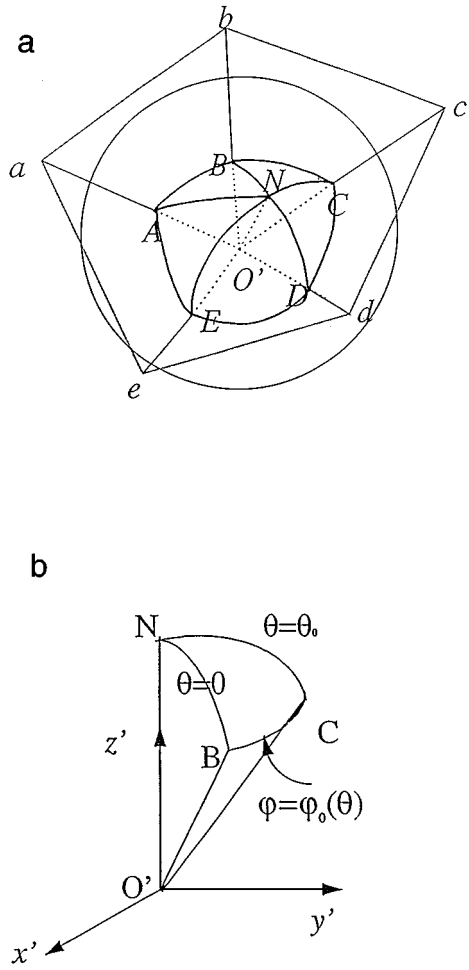

FIG. 4. (a) The part of a sphere contained in a corner. (b) A spherical triangle.

it a closed surface. But we found that in order to maintain a reasonable accuracy the size of the elements on the free surface and the artificial surfaces must be kept small so that the numerical integration will not introduce large errors. This will be very uneconomical in terms of computational time, and we do not wish to waste a lot of elements in the far field where very weak responses are expected. Here we adopt a direct approach based on the definition of solid angle, i.e., the area subtended by the linear elements on a unit sphere (cf. Fig. 4a). In Fig. 4a, $\widehat{AB}$, $\widehat{BC}$, $\widehat{CD}$, $\widehat{DE}$ and $\widehat{EA}$ are the diametral or geodesic arcs formed by the intersection of the unit sphere with the linear elements surrounding node point O', N is an arbitrary point on the sphere contained within the arcs on the side of the sphere where the area is measured. Here we choose N as the intersection point between the sphere and the normal direction calculated from the local surface-fitting scheme described earlier. $\widehat{AN}$, $\widehat{BN}$, etc. are geodesic arcs on the unit sphere linking N to the points A, B, respectively. Then the solid angle subtended by the linear elements around O' is just the sum of the areas of the spherical triangles *ANB*, *BNC*, etc. The formula to calculate the area of a spherical triangle is derived in Appendix A.

TABLE I
Maximum Errors Associated with the Computed Unit Normals as a Function of the Number of Nodes Used

Number of nodes	Maximum error (in degrees)
162	12.1
362	8.2
642	6.2
1002	4.9

3. RESULTS AND DISCUSSIONS

The computation was performed on a single-processor Silicon Graphics Power Challenger and a Cray J916 System. To maximize the efficiency, we used a nonuniform mesh on the free surface with a large number of elements concentrated in the regions immediately above the bubbles where a fine resolution is needed.

First we consider the convergence of the new model under mesh refinement. When there are no solid structures and free surface present in the fluid region, an initially spherical bubble periodically undergoes expansion and collapse motion, which can be described by the Rayleigh–Plesset equation and remains spherical in shape throughout its lifetime. We first test the accuracy and convergence of the surface-fitting scheme introduced in Section 2.1 by comparing the surface normals on the spherical bubble computed from our interpolation scheme with the analytical results. The maximum deviation of the computed normals (in terms of degrees) is tabulated in Table I for various resolutions. As can be seen in this table, the maximum deviation is brought down steadily as the mesh is refined and with a moderate number of nodes (642) being used, the computed normal directions are no more than 6° away from the true normal. The convergence of the interpolation scheme is thus verified.

Since the bubble remains spherical in shape throughout its lifetime, we can calculate its radius by computing its volume. Figure 5 shows the bubble radius as a function of time obtained from the 3D code with different resolutions and from the solution of the Rayleigh–Plesset equation using the fourth-order Runge–Kutta method. The numerical errors in the maximum bubble radius, which is 1 according to analytical solution, are tabulated in Table II. It is obvious from Fig. 5 and Table II that as the mesh is refined, the 3D solution converges quickly to the solution of the Rayleigh–Plesset equation; both the maximum bubble radius and the oscillation period are well predicted by the 3D model with no more than 1% error.

TABLE II
Numerical Errors Associated with the Computed Maximum Bubble Radius as a Function of the Number of Nodes Used

Number of nodes	Errors (%)
162	0.65
252	0.49
362	0.40

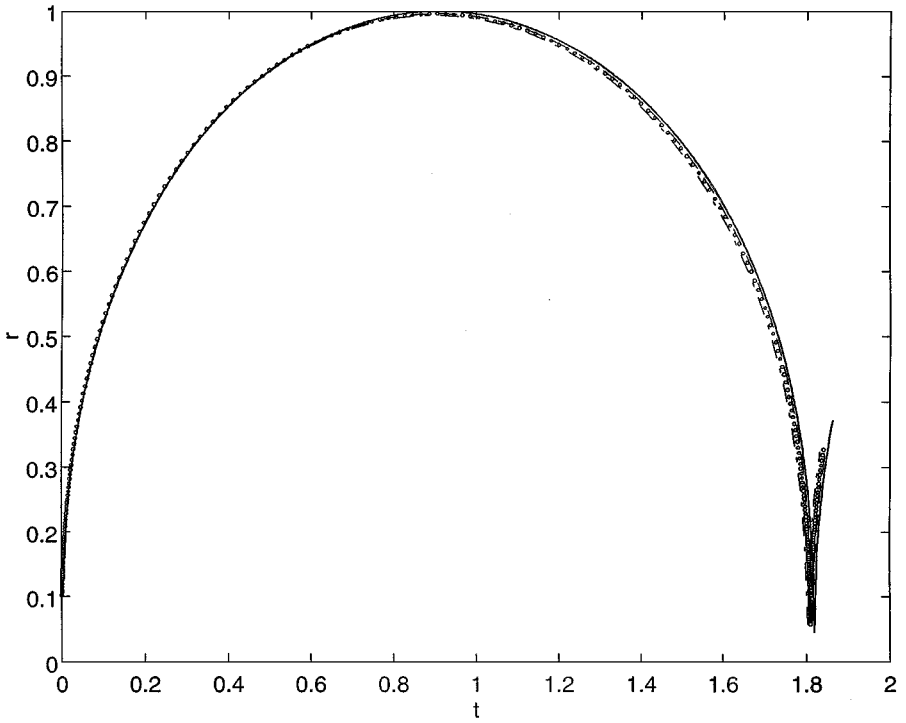

FIG. 5. Bubble radius as a function of time calculated from the new 3D model with 162 (dash-dotted line), 252 (circles), 362 (dash line) nodes on the bubble surface, and from the Rayleigh–Plesset equation (solid line).

Next we compare the results from the 3D code with those from the axisymmetric code developed by Wang *et al*. [14] for the case of a bubble initiated at one maximum radius below a free surface. Altogether 492 nodes were placed on the bubble surface and 1225 on the free surface. So there are roughly 43 nodes on a plane through the center of the bubble in the 3D run, compared to 101 nodes used in the axisymmetric code of Wang *et al*. For brevity only results near the final stage of the collapse phase are illustrated; see Fig. 6. Owing to the very large velocity of the reentrant jet at this point of the evolution, the time marching process slows to a virtual standstill because of the small time steps that must be maintained to ensure numerical stability. During the computation, we observe that the bubble calculated from the 3D code consistently evolves faster than its axisymmetric counterpart. This has resulted in a smaller bubble at the last stage of the collapse phase than that predicted by the axisymmetric model. This discrepancy might have resulted from the smoothing that has usually been applied in axisymmetric codes [2]. Also the free-surface hump calculated from the 3D code is 3% lower than that predicted by the axisymmetric code. On the whole, the bubble and the free-surface profiles, as well as the characteristics of the Bjerknes jet are all well predicted by the current 3D model, suggesting that the local interpolation scheme adopted here has worked well.

For further comparative testing, the configuration was simulated where a bubble is placed at a very large distance ($d = 5, 10, 20$ maximum bubble radius) from a solid wall. In this case, one would expect that the bubble motion should increasingly resemble that of the Rayleigh bubble at least during the expansion phase, and thus, the total expansion time should approach 0.915, the half period of a Rayleigh bubble. The total expansion time

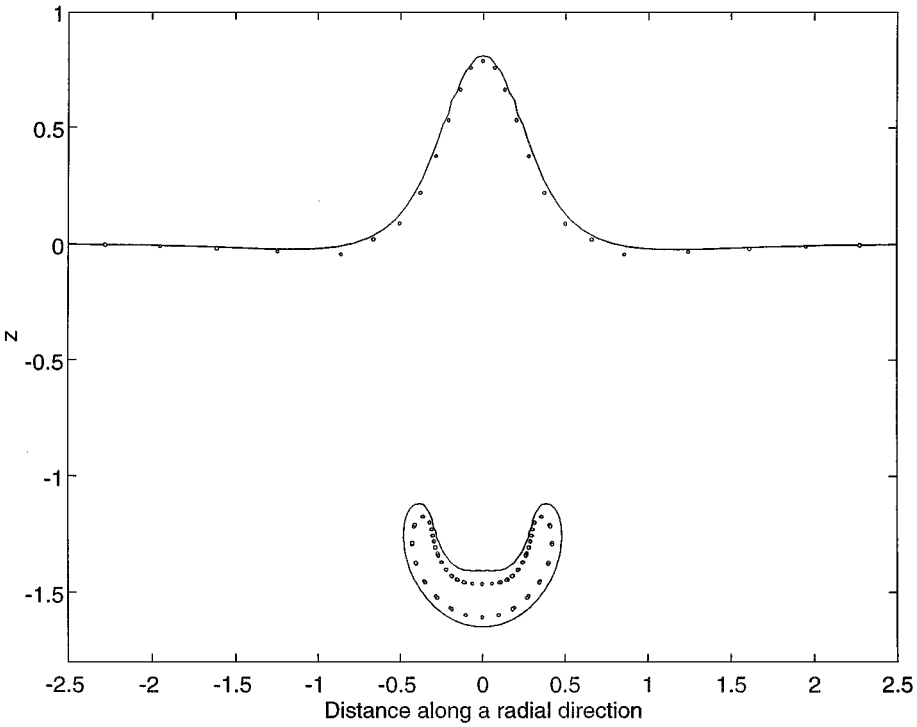

FIG. 6. Comparison of the bubble and free surface shapes for $\gamma = 1$ and $\delta = 0$ at $t = 1.4206$ calculated from our 3D code (circles) and an axisymetric code (solid lines).

calculated from the current 3D code is virtually indistinguishable from this value for $d = 10$ and 20, but the time obtained from the axisymmetric code is still 3.3%, 3%, and 0.4% larger than it for $d = 5, 10, 20$, respectively. In other words, the results from the axisymmetric model converge much slower than those from the 3D code. In the axisymmetric model of Wang *et al*. (as well as other axisymmetric models), artificial smoothing is indispensable in order to damp out the numerical instability, and this may have slowed down the bubble motion. On the other hand, no smoothing is required in the curent 3D model.

Adding a horizontal bottom below the bubble will affect the process, especially during the collapse phase, as noted by Wang *et al*. [14]. Note that the bottom needs not be discretized if a modified Green's function is used that takes into consideration of the reflected image of the source point. In Fig. 7a a comparison is made of the 3D and axisymmetric codes towards the final stage of bubbles collapse in a shallow water case. In this case, 642 nodes were placed on the bubble surface and 1521 on the free surface. The results from the two models again exhibit reasonable agreement although the bubble calculated from the 3D code is again a little smaller. The axisymmetric code virtually stopped at this time level $t = 1.4623$, but the 3D code was able to go further in time. The final sequence (Fig. 7b) shows the Bjerknes jet in its continued downward projection as a broad bulbous jet.

Having gained confidence on the performance of the new 3D code, we next proceed to consider a fully 3D case in which two identical bubbles are generated at the same horizontal level below a free surface. In the computation, we placed 492 nodes on each of the two bubbles and 1161 nodes on the free surface. The evolution of the bubbles and free surface is shown in Fig. 8. For this case, the bubbles eventually produce two spectacular spikes

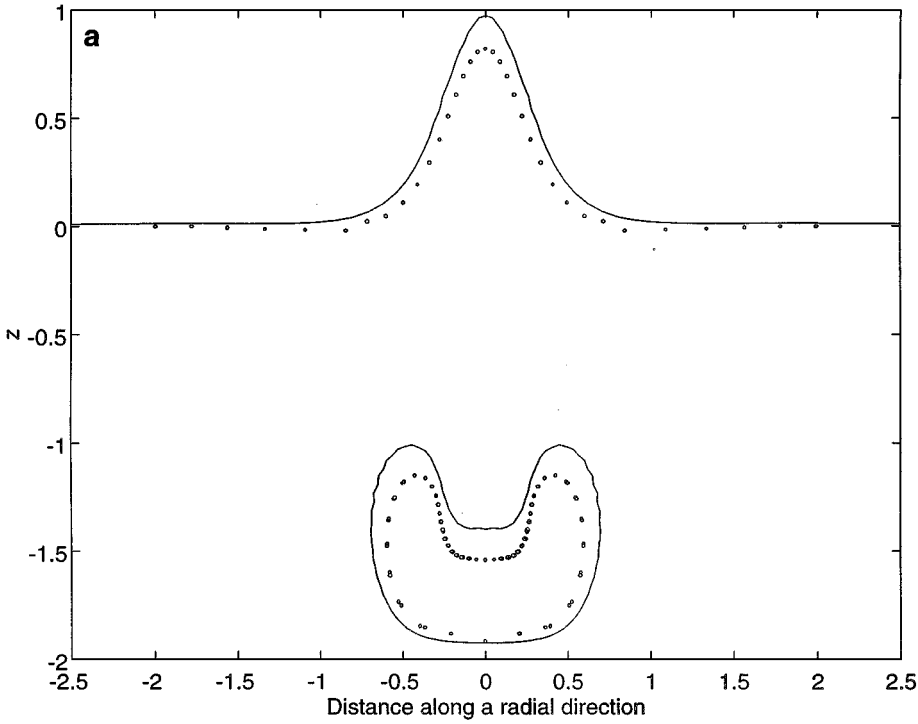

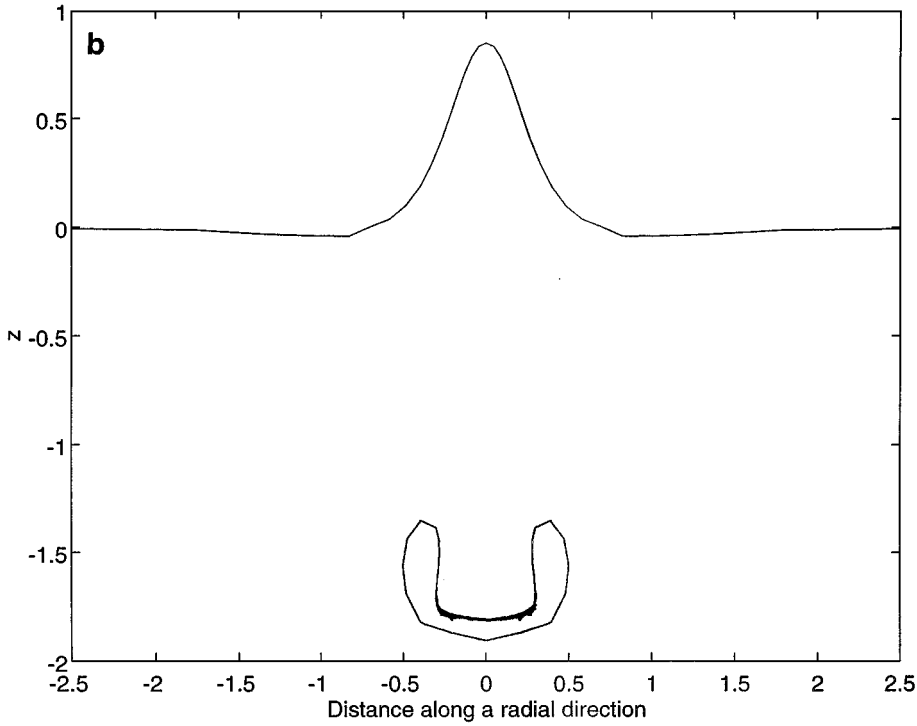

FIG. 7. Profile of the bubble and free surface in a shallow water calculated from our 3D code (circles) and an axisymetric code (solid lines), with $\gamma = 1$ and $\delta = 0$. The total depth is two maximum bubble radius: (a) $t = 1.4623$; (b) $t = 1.5454$.

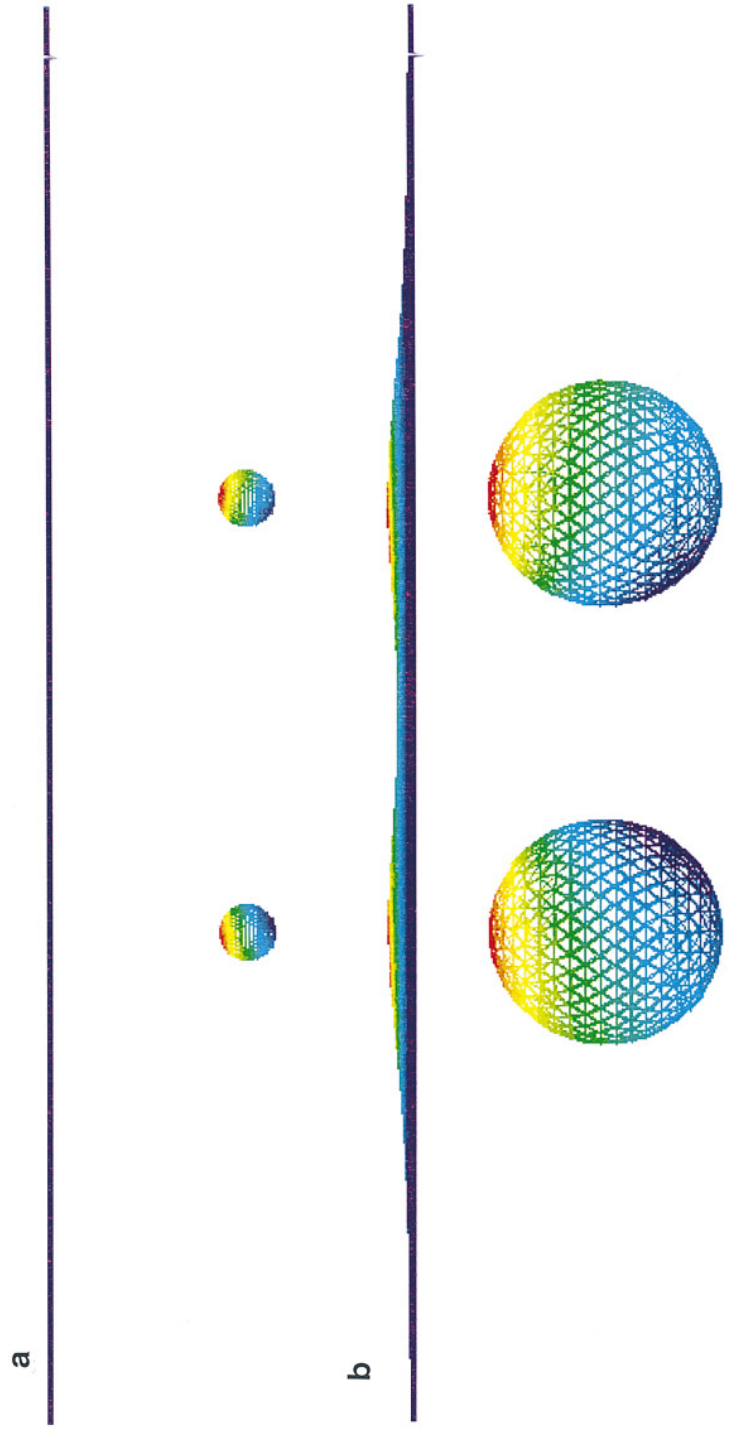

FIG. 8. Evolution of bubbles and free surface at dimensionless times: (a) 0.003445; (b) 0.1221; (c) 0.5981; (d) 1.1060; (e) 1.4438; (f) 1.4915. The initial distance between the two bubbles is 2.2.

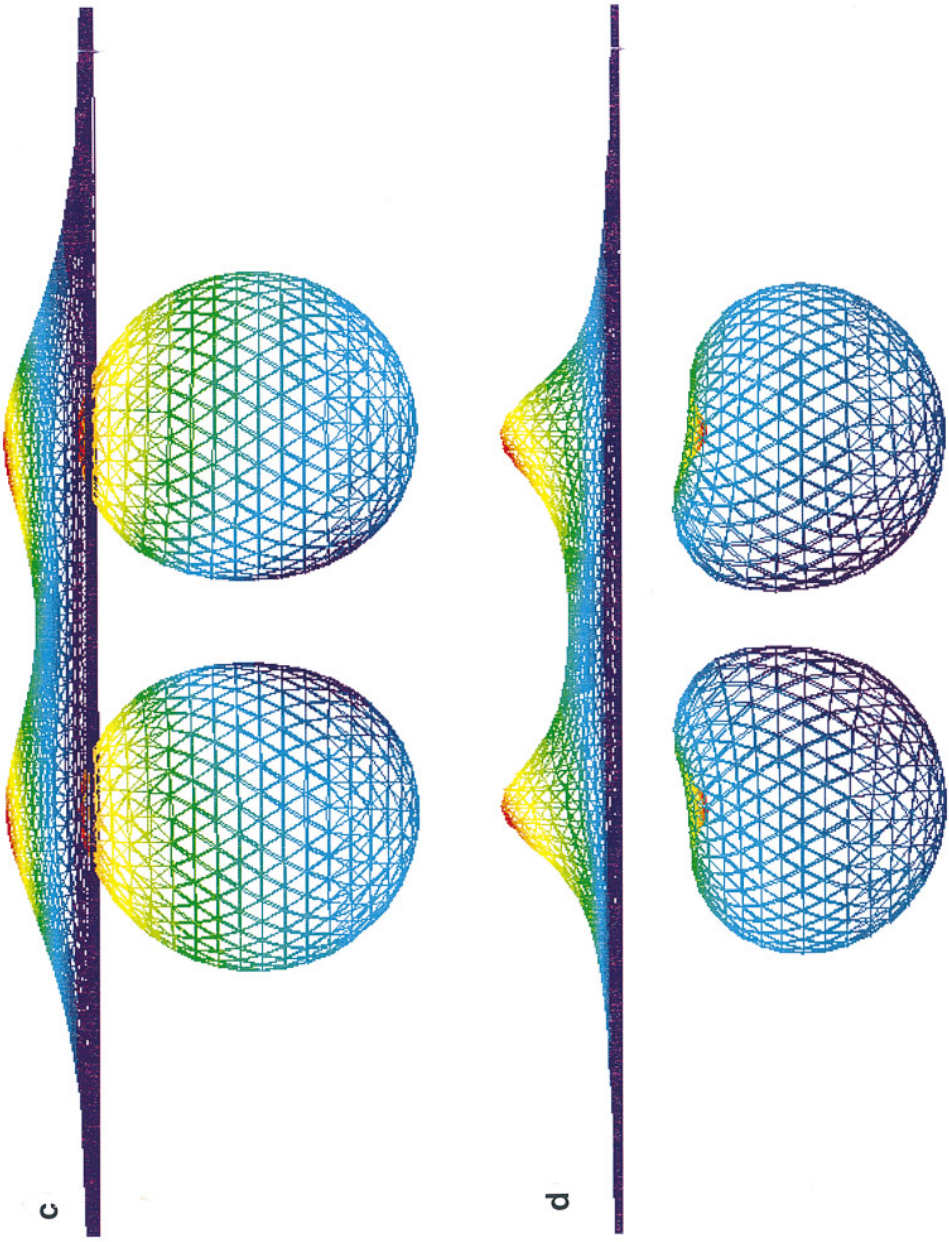

FIG. 8—*Continued*

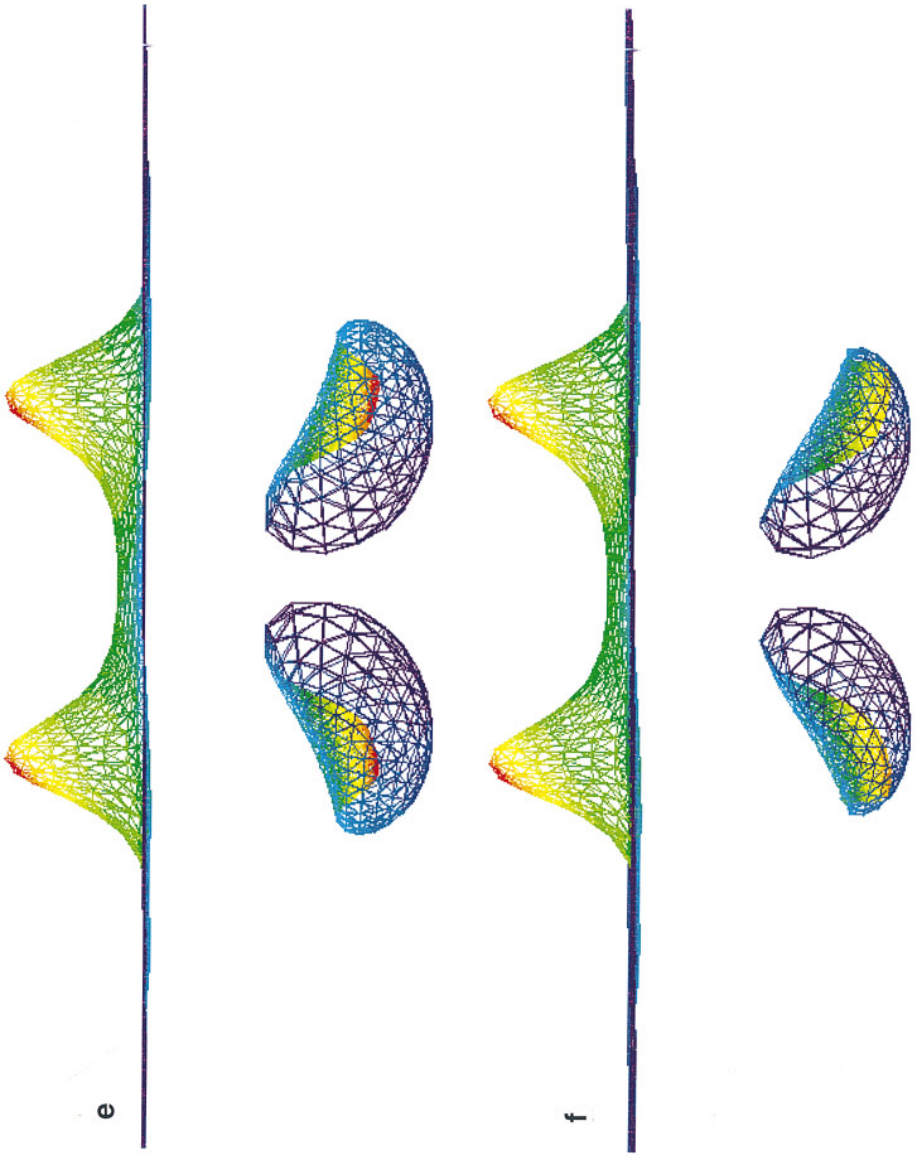

FIG. 8—*Continued*

on the free surface. The spikes are bridged by a broad valley elevated from the initially undisturbed free surface between the spikes. Steep slopes join the spikes to the quiescent plain of the far field. The Bjerknes jet which is formed at the beginning of the collapse phase moves obliquely downwards due to the combined effects of the free surface and the opposing bubble (or equivalently a solid wall placed at the symmetry plane). Depending on the relative magnitude of the repelling force from the free surface and the attraction force from the symmetry plane, different parts of the jet move in different directions: the part close to the symmetry plane moves towards it, whereas the part away from the symmetry plane moves mainly downwards. In the case presented here, the repelling force from the free surface seems to drive the jet stronger so that the jet penetrates the bubble at a point away from the symmetry plane.

No symmetry plane can be found in our next 3D example, in which two bubbles of different initial sizes are released at different depths below a free surface. The simulation was carried out with same amount of nodes being used on each of the two bubbles and the free surface as the in previous case. As can be seen in Fig. 9, the Bjerknes jet is only formed on the smaller bubble which is seeded nearer to the free surface, and above this bubble a big hump is raised on the free surface with a gentle slope trailing it on the side of the bigger bubble, a remnant of the other hump that would be present were it placed at a smaller distance from the free surface. The bigger bubble is still growing when the reentrant jet impacts the opposite wall of the smaller bubble and up to that point no reentrant jet is formed on the bigger bubble. This is not unexpected since the lifetime of a Rayleigh bubble is proportional to its maximum radius and the jetting only occurs near the end of the collapse phase. The formed jet is directed mainly downwards with a slight tilt towards the bigger bubble, a phenomenon also expected due to the attraction force from the bigger bubble.

4. CONCLUDING REMARKS

A new method to compute the material velocity on 3D bubbles and a free surface is proposed. The solid angle on the free surface is calculated by a direct method. The new procedure offers advantages over some of the existing 3D models. Our results compare favorably with corresponding results from the 1D Rayleigh–Plesset equation and an axisymmetric model. The 3D model has also been applied to some fully 3D cases involving the interactions of two bubbles and a free surface.

APPENDIX A: AREA OF A SPHERICAL TRIANGLE

It is convenient to adopt a local Cartesian coordinate system (x', y', z') (cf. Fig. 4b) and a spherical co-ordinate system (r, θ, φ) such that point N is the north pole and the arcs $\widehat{NB}$ and $\widehat{NC}$ are part of the longitude. The radius of the sphere is one. Referring to Fig. 4b, we then have the area of the spherical triangle NBC

$$S = \int_0^{\theta_0} \mathrm{d}\theta \int_0^{\varphi_0(\theta)} \sin\varphi \, \mathrm{d}\varphi = \theta_0 - \int_0^{\theta_0} \cos\varphi_0(\theta) \, \mathrm{d}\theta, \tag{A1}$$

where $\varphi = \varphi_0(\theta)$ represents the latitude of the arc $\widehat{BC}$, which is the intersection between the

plane $O'BC$

$$\begin{pmatrix} x' \\ y' \\ z' \end{pmatrix} = \begin{pmatrix} x'_B \\ y'_B \\ z'_B \end{pmatrix} s + \begin{pmatrix} x'_C \\ y'_C \\ z'_C \end{pmatrix} t, \tag{A2}$$

and the sphere

$$\begin{aligned} x' &= \cos\theta \sin\varphi, \\ y' &= \sin\theta \sin\varphi, \\ z' &= \cos\varphi, \end{aligned} \tag{A3}$$

with $0 \le \theta < 2\pi$ and $0 \le \varphi \le \pi$. From (A2) and (A3) we obtain

$$\cot\varphi_0(\theta) = \frac{z'_B(y'_C\cos\theta - x'_C\sin\theta) + z'_C(x'_B\sin\theta - y'_B\cos\theta)}{x'_B y'_C - x'_C y'_B}, \tag{A4}$$

and thus the integrand in (A1) can be obtained as

$$\cos\varphi_0(\theta) = \frac{\cot\varphi_0(\theta)}{\sqrt{1+\cot^2\varphi_0(\theta)}}. \tag{A5}$$

Although the integral in (A1) can be written in terms of elliptic integrals, we compute it via numerical means.

Since all the coordinates used here are local ones and points N, B, and C are not the original nodes, we also show how they can be linked to the original Cartesian coordinates of the original nodes B' and C'. From (A3), we only need to find the local spherical coordinates $\theta_C(=\theta_0)$, φ_B and φ_C ($\theta_B = 0$). Referring to Figs. 4a, b, we have

$$\cos\varphi_B = \mathbf{O'B}^0 \cdot \mathbf{O'N}^0 = \mathbf{O'B'}^0 \cdot \mathbf{O'N}^0, \tag{A6}$$

$$\cos\varphi_C = \mathbf{O'C}^0 \cdot \mathbf{O'N}^0 = \mathbf{O'C'}^0 \cdot \mathbf{O'N}^0, \tag{A7}$$

where the superscript "0" denotes the unit vector. The longitude of C can be calculated by noting that the dot product $\mathbf{O'B'}^0 \cdot \mathbf{O'C'}^0$ is invariant under the change of coordinate system. Therefore, we have

$$\sin\varphi_B \sin\varphi_C \cos\theta_C + \cos\varphi_B \cos\varphi_C = \mathbf{O'B'}^0 \cdot \mathbf{O'C'}^0 \tag{A8}$$

and, hence,

$$\cos\theta_C = \frac{\mathbf{O'B'}^0 \cdot \mathbf{O'C'}^0 - \cos\varphi_B \cos\varphi_C}{\sin\varphi_B \sin\varphi_C}. \tag{A9}$$

Once θ_C, φ_B, and φ_C are found, (x'_B, y'_B, z'_B) and (x'_C, y'_C, z'_C) can be found from (A3). Note that the coordinates of the point N are immaterial once the normal vector $\mathbf{O'N}^0$ is found from the local surface interpolation scheme.

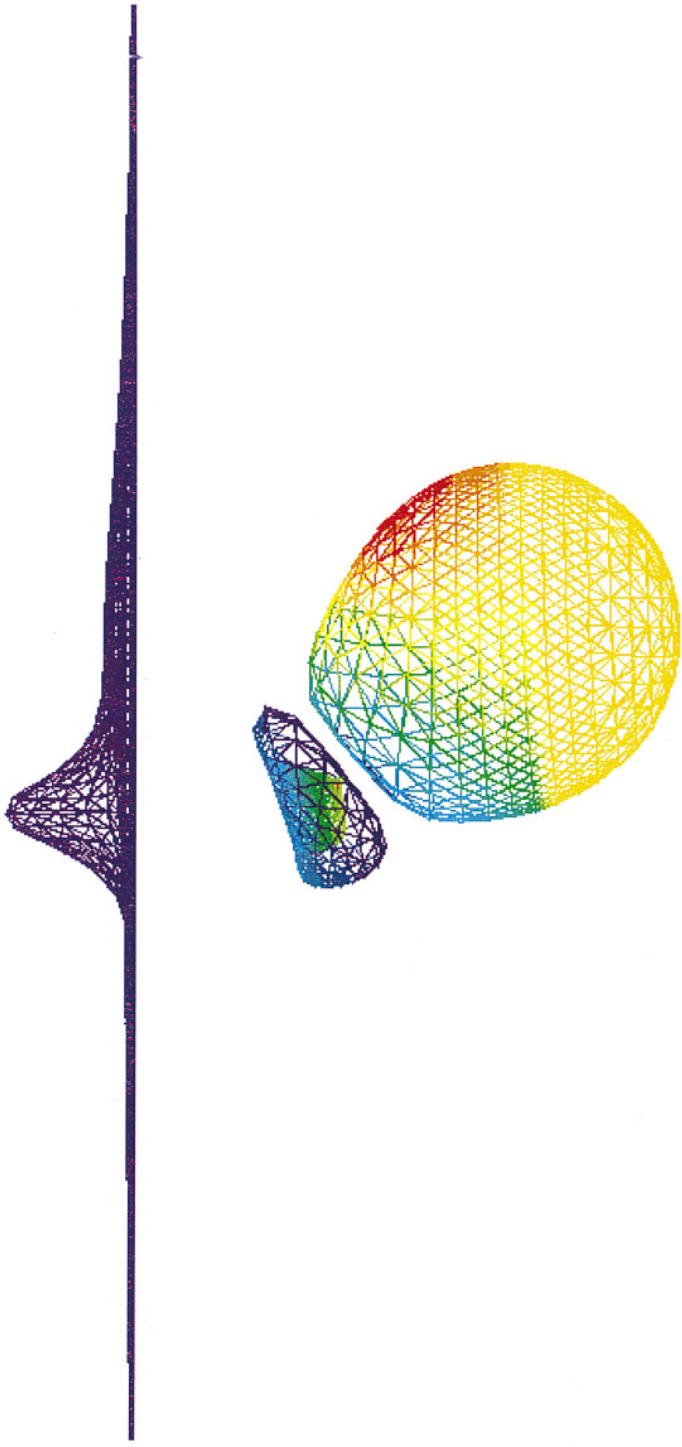

FIG. 9. Final profiles of the free surface and bubbles at $t = 1.1715$. The initial radii of the two bubbles are 0.05 and 0.1, respectively, with the distance between them being 1.6. The smaller bubble is placed at a distance of 0.8 from the free surface, and the bigger bubble 2.049.

REFERENCES

1. P. J. Harris, A numerical model for determining the motion of a bubble close to a fixed rigid structure in a fluid, *Int. J. Numer. Methods Eng.* **33**, 1813 (1992).
2. J. R. Blake, J. M. Boulton-Stone, and R. P. Tong, Boundary integral methods for rising, bursting and collapsing bubbles, in *BE Applications in Fluid Mechanics, 1995*, edited by H. Power, Vol. 4, p. 31.
3. G. L. Chahine, T. O. Perdue, and C. B. Tucker, Interaction between an underwater explosion bubble and a solid submerged body, Traycor Hydronautics, Inc., Technical Report 86029-1, 1988.
4. G. L. Chahine and T. O. Perdue, Simulation of the three-dimensional behavior of an unsteady large bubble near a structure, in *Drops and Bubbles, A.I.P. Conference Proceedings, 1989*, edited by T. G. Wang, p. 169.
5. A. Z. Zinchenko, M. A. Rother, and R. H. Davis, A novel boundary-integral algorithm for viscous interaction of deformable drops, *Phys. Fluids* **9**, 1493 (1997).
6. S. A. Wilkerson, *A Boundary Integral Approach to Three Dimensional Underwater Explosion Bubble Dynamics*, Ph.D. dissertation, Johns Hopkins University, Baltimore, MD, 1990.
7. G. L. Chahine, Numerical modelling of the dynamic behavior of bubble in nonuniform flow fields, in *ASME Symposium on Numerical Method for Multiphase Flows, Toronto, 1990*.
8. P. J. Harris, A numerical method for predicting the motion of a bubble close to a moving rigid structure, *Commun. Numer. Methods Eng.* **9**, 81 (1993).
9. J. R. Blake and R. P. Tong, Jet impact in collapsing bubbles, in *12th Australian Fluid Mechanics Conference, The University of Sydney, 1995*, Vol. 2, p. 819.
10. L. Chen, J. A. Reizes, and E. Leonardi, A numerical study of bubble motion in a gravitational field, in *12th Australian Fluid Mechanics Conference, The University of Sydney, 1995*, Vol. 2, p. 827.
11. C. A. Brebbia, J. C. F. Telles, and L. C. Wrobel, *Boundary Element Techniques* (Springer-Verlag, New York/Berlin, 1984).
12. D. C. Gibson and J. R. Blake, The growth and collapse of bubbles near deformable surfaces, *Appl. Sci. Res.* **38**, 215 (1982).
13. G. L. Chahine and R. Duraiswami, Dynamical interactions in a multi-bubble cloud, *Trans. ASME* **114**, 680 (1992).
14. Q. X. Wang, K. S. Yeo, B. C. Khoo, and K. Y. Lam, The evolution of a gas bubble in a shallow water, *in 12th Australian Fluid Mechanics Conference, The University of Sydney, 1995*, Vol. 2, p. 823.
15. J. R. Blake, B. B. Taib, and G. Doherty, Transient cavities near boundaries. Part 1. Rigid boundary, *J. Fluid Mech.* **170**, 479 (1986).
16. J. R. Blake, B. B. Taib, and G. Doherty, Transient cavities near boundaries. Part 2. Free surface, *J. Fluid Mech.* **181**, 197 (1987).
17. T. J. R. Hughes, *The Finite Element Method* (Prentice-Hall, Englewood Cliffs, NJ, 1987).